ingegneria sismica
International Journal of Earthquake Engineering
Anno XLIII - Num. 2 - 2026

Model and solution of grounding "red light band" problem for 25Hz phase-sensitive track circuit

Jingteng Fan[1,2], *Wudong Yang*[1] *and Yi Zhang*[1,*]

[1] School of Information Science and Technology, Southwest Jiaotong University, Chengdu 611756, Sichuan

[2] Chengdu Turboost Railway Signal Technology Co. Ltd., Chengdu 610041, Sichuan

SUMMARY: *In view of the "red light band" phenomenon of 25 Hz phase-sensitive track circuit under the condition of maintenance and grounding, this paper constructed a computational analysis framework for abnormal identification and disposal output. Based on the six-terminal network transmission relationship, the section length, ballast resistance, reflux Settings and ground point position are written into the state space. The finite difference and cascaded recurrence methods are used to solve the track voltage of the receiving end, and the unified structure of grounding anomaly feature representation is constructed. The experiment covers three sections of 1.2 km, 0.6 km and 0.3 km, and two ballast resistance conditions of 0.6 Ω·km and 6.0 Ω·km. The results show that the reflux setting determines the location of abnormal occurrence, and the section length and ballast resistance affect the scope of the release area. The proposed dual-rail impedance grounding scheme makes the average reduction of rail voltage after grounding be 5.230%, the average experimental voltage reach 14.284V, the average relative error is -1.310%, and the mean square error is 2.139%.*

KEYWORDS: *25Hz phase-sensitive track circuit; Ground red light band; Finite difference solution; Computational diagnosis*

1 Introduction

With the improvement of station electrification, train density and equipment linkage level, the operation stability of 25Hz phase-sensitive track circuit in section occupancy inspection is constrained. During the outage maintenance of the traction network, the original signal transmission path will be changed after the ground line is connected to the rail, and the additional coupling branch will appear in the rail loop, and the voltage at the receiving end will decrease. When the voltage is close to or below the relay release threshold, the idle section will show the occupancy display on the console, which will affect the route management, interlocking logic and maintenance organization in the station. This phenomenon is closely related to the section length, ballast resistance and reflux setting conditions. It is more likely to occur under the joint action of short section, high ballast resistance and unilateral reflux channel. Therefore, it is necessary to describe the relationship between signal loop, electrical boundary and ground disturbance with a computable model.

The 25Hz phase-sensitive track circuit assumes the task of continuous, low frequency and strong constraint discrimination. Its running state is not only affected by the matching of the

*keitou723@163.com
https://doi.org/10.65102/is2026506 Published: 30 April, 2026

transmitter, the distribution parameters of the rail, the connection mode of the choke transformer, but also restricted by the reconstruction of the temporary ground loop under the maintenance condition. The traditional treatment methods mainly start from the adjustment of operating position, field trial and local equipment modification, which can alleviate the voltage sag in individual scenarios, but it is difficult to directly answer the computational questions of how the rail voltage changes after grounding under different boundary conditions, how the most unfavorable combination is formed, and which grounding parameters can meet the calculation of signal transmission and personal protection at the same time. Only by transforming field phenomena into state variables, transmission relations and verifiable outputs, can a research framework connected with information processing, intelligent diagnosis and engineering computing be formed.

Focusing on the intelligent analysis of railway signal equipment, Lian et al studied the application of artificial intelligence in railway signal interlocking fault [1]. Yang studied the implementation path of improved FP-Growth algorithm in fault diagnosis of railway signaling equipment [2]. Hu et al. reviewed the data-driven fault diagnosis technology of switch machine [3]. Li et al. proposed a fault diagnosis method of turnout system combining improved autoencoder and data augmentation [4]. Cao et al. studied the fault recognition method of switch machine based on sound signal and ensemble classifier [5]. Sun et al. proposed a non-contact diagnosis method based on multi-scale fractional wavelet packet energy entropy [6]. Cao et al. further proposed the application of deep random forest fusion model in the diagnosis of point machine [7]. Chen et al. studied the railway turnout fault recognition method combining multi-head channel self-attention and deep convolutional network [8]. Sun et al. proposed a condition monitoring and fault diagnosis strategy for vibration signal monitoring [9]. Zhang et al. studied the application of parameter optimized VMD and integrated feature selection in signal relay defect detection [10]. These results show that computer technology has penetrated into the feature modeling, deep representation and diagnosis process of railway signaling equipment.

The existing research is more oriented to the state recognition of point machines, relays and general signal equipment. The data form is mainly text, sound and vibration sequence, and the "red light band" phenomenon under the ground condition has different mechanism characteristics. This kind of phenomenon is not a static discrimination of ordinary failure samples, but a dynamic voltage sag process triggered by the traction supply connection, rail distribution parameters and boundary port conditions.

Based on the above background, this paper discretizes the track circuit state under the ground condition into computable samples, and constructs a modeling process for the identification and disposal of "red light band". In the method, a six-terminal network is introduced to express the transmission relationship between the transmitter, the ground and the receiver. The finite difference and cascaded recurrence are used to solve the track voltage, and the section length, ballast resistance, reflux setting and ground position are encoded as state variables. At the diagnosis level, the intelligent computing model of the grounding scene was established by abnormal signal representation, key feature extraction and discriminant output. At the disposal level, the verification link is constructed by combining the impedance grounding scheme, so that the model output can serve the solution selection and effect evaluation. The rest of this paper is arranged as follows: Section 2 combs the related work, Section 3 introduces the grounded "red light band" research method, Section 4 gives the result analysis, and Section 5 gives the conclusion.

2 Related work

This section focuses on intelligent diagnosis of railway signaling equipment, track circuit transmission modeling, and anomaly display analysis under maintenance and grounding conditions. Existing research has formed technical routes in data mining, deep representation, rule-based reasoning and few-shot identification. However, for the "red band" phenomenon after 25Hz phase-sensitive track circuit grounding, it is still more necessary to link the deft level diagnosis method with the track voltage transmission mechanism.

Li and Mu studied the analysis platform of rail transit vehicle signal system based on data mining, focusing on operation and maintenance data aggregation, state recognition and platform analysis [11]. Zhou and Li studied the fault diagnosis method of computer interlocking system, associating the interlocking logic in railway signal control with the fault judgment process [12]. Wang et al. proposed a diagnosis method of high-speed railway turnout based on piecewise mRMR feature selection and cost-sensitive extreme learning machine, which enhanced the recognition ability under the condition of class imbalance [13]. Heinrich et al. studied the rule-based anomaly detection mechanism in the railway signaling network, which makes the anomaly identification of the network layer interpretable [14]. Chen et al. proposed a subway turnout fault detection method based on convolutional autoencoder, and used deep feature compression for equipment state discrimination [15]. Lao et al. studied a few-sample turnout diagnosis method combined with semi-supervised weighted prototype network, which made the model training under the condition of limited samples more adaptive [16]. Reetz et al. proposed an expert system diagnosis framework for railway switching equipment, which combines knowledge rules with fault reasoning [17]. Xiao et al. studied the switch intelligent diagnosis method based on deep reinforcement learning, and introduced the dynamic decision-making mechanism into the process of equipment state recognition [18]. Yang et al. proposed a railway signal equipment diagnosis method combining data enhancement and improved attention mechanism, which improved the ability to capture key patterns in the feature extraction stage [19]. Sugiana et al. studied the identification method of railway turnout state based on current signals and machine learning, which provided a reusable idea for equipment diagnosis driven by electrical features [20].

From the existing results, the intelligent analysis of railway signals has formed a technical pattern of platform analysis, rule detection, deep representation and adaptive learning in parallel. To illustrate the connection between these studies and the object of this paper, as shown in Table 1, although existing methods vary in input types and modeling ways, most of them focus on dep-level identification tasks, while the ground "red light band" scenario also involves backflow boundaries, track distribution parameters, and voltage threshold linkage.

Table 1: Comparison of focus points between research on intelligent diagnosis of railway signals and research on grounding scene modeling

Research Direction	Representative Methods	Input Types	Main Focus
Signal System Analysis	Data Mining, State Statistics	Logs, Operation and Maintenance Records	Platform-Based Monitoring and State Aggregation
Interlocking and Network Anomaly Detection	Rule Reasoning, Fault Diagnosis	Interlocking Events, Network Behaviors	Logical Anomaly Identification and Alarm Generation
Intelligent Diagnosis of Turnout Equipment	Feature Selection, Deep Networks, Few-Shot Learning	Vibration, Sound, Current	Equipment-Level Recognition Accuracy
Grounding-Induced “Red Light Band” Modeling	Six-Terminal Network, Finite Difference, Recursive Solution	Section Parameters, Return Current Conditions, Grounding Points	Rail Voltage Transmission and Scheme Verification

However, the "red light band" phenomenon after the track circuit is grounded is not the same as the general equipment failure. Most of the previous studies regard the diagnosis object as a relatively independent device unit, and the model focuses on feature classification, anomaly recognition or state alarm. The input data mainly come from text, vibration, current, sound and operation log. When the 25Hz phase-sensitive track circuit shows abnormal display under the condition of maintenance and grounding, the result is determined not only by the degradation state of a local device, but also by the combined effect of the transmitter impedance, the receiver load, the rail distribution parameters, the choke connection mode, the ground point location and the reflux boundary. In other words, such scenarios contain both computable transport processes and discriminative state outputs. If only the general diagnostic model is used and the mechanism calculation of rail voltage is missing, the model can give abnormal conclusions, but it is difficult to explain why the voltage sag amplitude changes under different section lengths, different ballast resistance and different reflux Settings.

Therefore, existing related work has already provided the basis for this paper in two aspects. On the one hand, research on intelligent diagnosis of railway signaling equipment has proved that feature modeling, deep learning, rule reasoning and data augmentation can improve the ability of anomaly recognition. On the other hand, the track circuit transmission analysis shows that the track voltage variation under complex operating conditions must be described by parametric modeling and numerical solution. The work of this paper is at the intersection of these two research lines, that is, the anomaly display after the grounding of the 25Hz phase-sensitive track circuit is transformed into a discrete, computable and verifiable modeling object. On the basis of the mechanism analysis, the state feature organization, the abnormal signal representation and the disposal plan evaluation are introduced, so that the "red band" recognition can not only indicate whether the anomaly is present, but also indicate whether the anomaly is present. It can also explain how anomalies form and which solutions are more suitable for field remediation.

3 Research Methods

3.1 Sample Construction and state modeling of 25Hz phase-sensitive track circuit grounding "red light band" problem

The 25Hz phase-sensitive track circuit ground "red light band" scenario is not a pure result discrimination process. The sample construction needs to simultaneously preserve the joint effect of ground position, reflux connection, section scale, ballast state and port impedance on track voltage. Based on this understanding, in this section, the maintenance grounding conditions are discretized into computable samples, and the electrical parameters, topological relationships and threshold discriminant information are organized in the state space to provide a unified input for subsequent anomaly representation and intelligent inference.

After the ground scene identification and boundary point definition are completed, the sample state can not only be discretized according to the ground position or the backflow mode, but also need to write the continuous transmission relationship between the dual-rail potential, current and port impedance into a computable expression. In this paper, a six-terminal network transmission model is used to describe the state propagation of the track circuit under the ground condition. On this basis, the finite difference recurrence form is introduced to discretize the continuous rail into computable units, so that the subsequent sample coding, state update and diagnosis output are based on a unified transmission relationship.

$$\begin{cases} \dfrac{dU_{1x}}{dx} = z_1 I_{1x} + z_{12} I_{2x} \\ \dfrac{dU_{2x}}{dx} = z_{12} I_{1x} + z_2 I_{2x} \\ \dfrac{dI_{1x}}{dx} = (g_1 + g_{12}) U_{1x} - g_{12} U_{2x} \\ \dfrac{dI_{2x}}{dx} = (g_2 + g_{12}) U_{2x} - g_{12} U_{1x} \end{cases} \tag{1}$$

where, U_{1x} and U_{2x} respectively represent the ground potential of two rails at any position x of the rail surface, and I_{1x} and I_{2x} respectively represent the corresponding rail current. z_1 and z_2 represent the distributed impedance of the two rails per unit length, z_{12} represent the distributed mutual impedance between the rails, g_1 and g_2 represent the distributed conductance of the two rails to the ground, and g_{12} represent the distributed transconductance between the two rails formed by the surface leakage of the track bed. Equation (1) gives the basic transmission law of sample states in continuous space, which is also the basis for subsequent discretization modeling.

In order to ensure that the sample source was consistent with the field working conditions, the sample generation phase extracted structural variables according to the actual connection relationship of the maintenance and grounding in the station, and then transcribed the electrical path between the transmitter, the ground and the receiver into a computable unit. Fig. 1 shows the basic scenario of detoured branch caused by maintenance grounding, which corresponds to three discrete conditions in the sample definition: reflux mode, ground point location and whether the rail surface channel is closed.

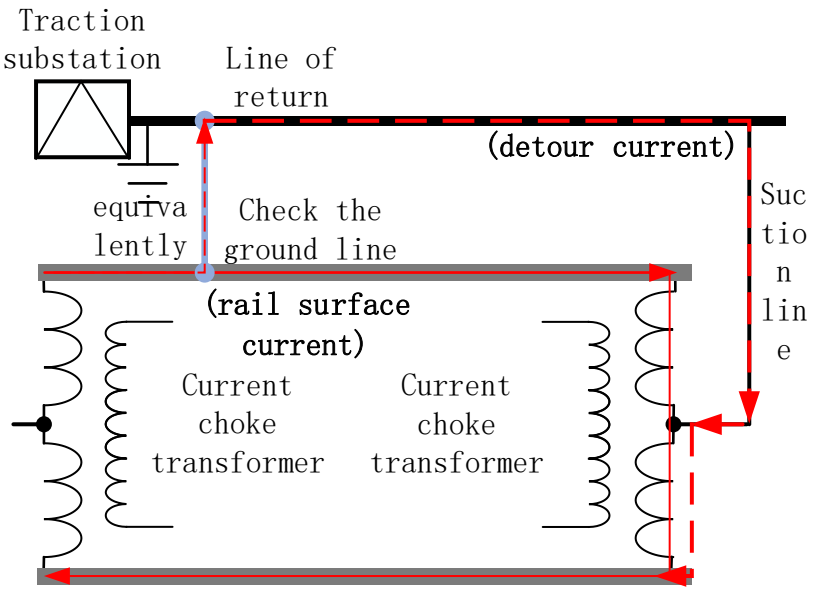

Figure 1: Schematic diagram of the grounding operation

As shown in Fig. 2, the sample states are no longer recorded by a single point of failure, but are organized by the overall transmission relationship of the track section. The sending point, both sides of the ground point and the receiving point together form the state boundary, the double rail potential, current and port impedance form the state component, and the

section length and the ballast resistance are used as external constraints to enter the modeling process. This organization can map the structural changes in the maintenance conditions directly into the calculation graph.

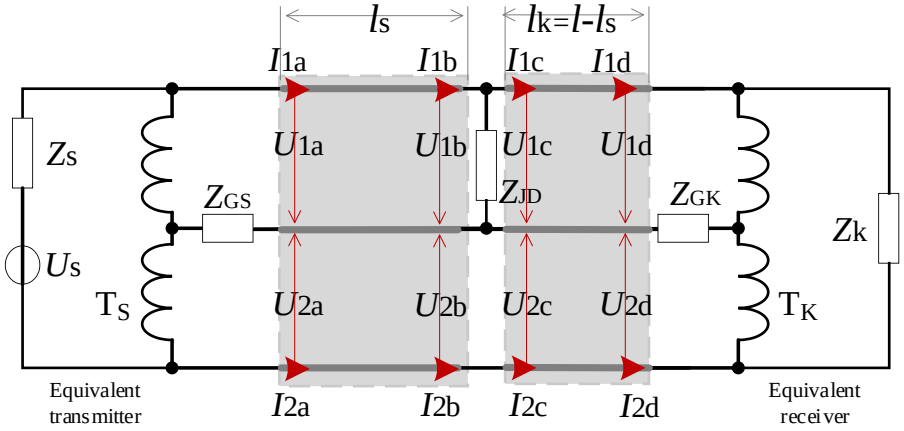

Figure 2: Track circuit grounding model based on six-terminal network

In order to make the transmission relation directly enter the calculation process, the rail with length l is divided into finite segment elements according to the step Δx, and the state propagation between adjacent elements is written in a recursive form. After this processing, the ground "red light band" samples can be transformed from continuous field variables into state vector sequences, which is convenient for subsequent model input and numerical solution.

$$\begin{bmatrix} U_1^{(i+j)} \\ U_2^{(i+j)} \\ I_1^{(i+j)} \\ I_2^{(i+j)} \end{bmatrix} = A^{-j} \begin{bmatrix} U_1^{(i)} \\ U_2^{(i)} \\ I_1^{(i)} \\ I_2^{(i)} \end{bmatrix} \tag{2}$$

$$A = \begin{bmatrix} 1 & 0 & z_1\Delta x & z_{12}\Delta x \\ 0 & 1 & z_{12}\Delta x & z_2\Delta x \\ (g_1+g_{12})\Delta x & -g_{12}\Delta x & 1 & 0 \\ -g_{12}\Delta x & (g_2+g_{12})\Delta x & 0 & 1 \end{bmatrix} \tag{3}$$

Here, A is the recurrence coefficient matrix, i represents the equivalent cell position of the current rail surface, and j represents the number of offset lengths spanned. Equations (2) and (3) rewrite the continuous distributed parameter network into an executable matrix recurrence relation, which can directly support batch calculation of samples, state return and unified comparison under different working conditions.

In the grounded sample, the sender, both sides of the ground and the receiver constitute the critical boundaries for state propagation. According to the segment length and the ground position, the state propagation from the transmitter to the front side of the ground point and from the back side of the ground point to the receiver can be expressed by the recurrence matrix respectively, so that different ground position samples can be integrated into the same modeling framework.

$$\begin{bmatrix} U_{1b} \\ U_{2b} \\ I_{1b} \\ I_{2b} \end{bmatrix} = A^{-N_s} \begin{bmatrix} U_{1a} \\ U_{2a} \\ I_{1a} \\ I_{2a} \end{bmatrix} \tag{4}$$

$$\begin{bmatrix} U_{1d} \\ U_{2d} \\ I_{1d} \\ I_{2d} \end{bmatrix} = A^{-N_k} \begin{bmatrix} U_{1c} \\ U_{2c} \\ I_{1c} \\ I_{2c} \end{bmatrix} \tag{5}$$

Here, $N_s = l_s/\Delta x$, $N_k = l_k/\Delta x$, and l_s and l_k denote the distance from the ground point to the transmitter and receiver, respectively. Equations (4) and (5) divide the track section into front and back parts according to the ground point, so that the ground point is no longer just the field operation location, but the core structural variable entering the sample state space.

After the interval recursion is completed, the sample state must also satisfy the port constraints of the sender, receiver, and ground point. Only when the boundary voltage, current and ground impedance are uniformly written into the port condition, the model can completely reflect the formation process of track voltage drop under the grounding condition and keep consistent with the actual electrical connection relationship.

$$\begin{cases} (U_{1a} - U_{2a}) + \dfrac{Z_s}{2}(I_{1a} - I_{2a}) = U_s \\ (U_{1d} - U_{2d}) - \dfrac{Z_k}{2}(I_{1d} - I_{2d}) = 0 \\ U_{1a} + U_{2a} + 2Z_{GS}(I_{1a} + I_{2a}) = 0 \\ U_{1d} + U_{2d} - 2Z_{GK}(I_{1d} + I_{2d}) = 0 \\ U_{1b} - U_{1c} = 0 \\ U_{2b} - U_{2c} = 0 \\ I_{1b} - I_{1c} - \dfrac{U_{1c}}{Z_{JD}} = 0 \\ I_{2b} - I_{2c} = 0 \end{cases} \tag{6}$$

Here, U_s represents the transmit supply voltage, Z_s represents the transmit impedance, Z_k represents the equivalent load at the receiver, Z_{GS} and Z_{GK} represent the impedance of the balanced coils at both ends to the reference ground, respectively, and Z_{JD} represents the ground impedance. After the port conditions are explicitly written into the state space in Equation (6), the track circuit ground sample has a complete boundary description ability.

Based on the above recurrence relations and port constraints, the overall transmission expression between the sending point and the receiving point can be further established. The expression is used to directly relate the input and output of the sample, so that the track voltage at the receiver can be used as a unified output for subsequent anomaly discrimination and solution verification.

$$\begin{bmatrix} U_{1d} \\ U_{2d} \\ I_{1d} \\ I_{2d} \end{bmatrix} = A^{-N_k} J^{-1} A^{-N_s} \begin{bmatrix} U_{1a} \\ U_{2a} \\ I_{1a} \\ I_{2a} \end{bmatrix} \tag{7}$$

$$J = \begin{bmatrix} 1 & 0 & 0 & 0 \\ 0 & 1 & 0 & 0 \\ Z_{JD}^{-1} & 0 & 1 & 0 \\ 0 & 0 & 0 & 1 \end{bmatrix} \tag{8}$$

Here, J is the grounding condition coefficient matrix, which is used to characterize the local connection relationship after the introduction of the ground point. Equations (7) and (8) incorporate the grounding disturbance into the unified transmission link, so that the samples can simultaneously reflect the coupling influence between the segment parameters, the grounding position and the boundary port.

After the construction of the recurrence relation and the definition of the ground condition matrix, it is still necessary to write the transmitter input, the receiver boundary constraint, and the ground branch correction into the same solution equation in a unified way. Based on the above transmission link and port conditions, the overall matrix expression of the track circuit in the ground state can be further sorted out, and the comprehensive solution relationship is shown in Equations (9) to (11).

$$\begin{bmatrix} 1 & -1 & Z_s/2 & -Z_s/2 \\ 1 & 1 & 2Z_{GS} & 2Z_{GS} \\ \Psi_{11} & \Psi_{12} & \Psi_{13} & \Psi_{14} \\ \Psi_{21} & \Psi_{22} & \Psi_{23} & \Psi_{24} \end{bmatrix} \begin{bmatrix} U_{1a} \\ U_{2a} \\ I_{1a} \\ I_{2a} \end{bmatrix} = \begin{bmatrix} U_s \\ 0 \\ 0 \\ 0 \end{bmatrix} \tag{9}$$

$$\Psi = H \times A^{-N_k} \times J^{-1} \times A^{-N_s} \tag{10}$$

$$H = \begin{bmatrix} 1 & -1 & -Z_k/2 & Z_k/2 \\ 1 & 1 & -2Z_{GK} & -2Z_{GK} \end{bmatrix} \tag{11}$$

Here, Ψ_{ij} is the element in row i and column j of matrix Ψ, Ψ represents the comprehensive transmission matrix after the joint effect of the receiver constraint and the ground transmission link, H is the boundary condition matrix of the receiver, A^{-N_s} and A^{-N_k} represent the recursive transmission relationship between the sending point and the front side of the ground point, and between the back side of the ground point and the receiving point, respectively. J^{-1} represents the local connection correction term after the grounding condition is introduced. Equations (9) to (11) unify the transmitter input, rail transmission, ground disturbance, and receiver constraints into the same matrix equation, thus completing the closure of the solution chain of the track circuit state in the grounded "red light band" scenario.

Through the above process of sample construction and state modeling, the section parameters, ground point locations, reflux Settings, and port impedance relationships of the 25Hz phase-sensitive track circuit under ground conditions are uniformly written into the same computational framework, and the originally scattered field conditions are transformed into recursive, solvable, and comparable state expressions. After processing in this way, the variation of the track voltage at the receiver no longer stays at the phenomenon level, but can correspond to explicit transmission paths and boundary constraints in the sample space. The resulting state matrix not only retains the electrical coupling characteristics of the ground "red light band" scene, but also provides a stable data basis for subsequent ground fault feature extraction, abnormal signal representation and diagnostic output.

3.2 Ground fault feature extraction and track circuit abnormal signal representation

After the grounding condition sample construction and state modeling, the input data of the track circuit has the basic attributes of section length, ballast resistance, reflux setting, ground point location and port impedance, but these raw quantities still stay in the electrical parameter layer and cannot directly enter the abnormal identification process. After this process, the ground "red light band" is no longer just a field display result, but can correspond to a set of numerical vectors with physical meaning and discriminative direction in the feature space.

In order to ensure the comparability of the grounding samples under different section conditions, the feature extraction link first normalized the receiver voltage, rail surface potential difference and section position variables, and then transcribed the reflux setting and grounding mode into discrete codes. After unified coding, samples under different working conditions can be mapped to the same feature space, so as to avoid the deviation caused by dimensional differences for subsequent abnormal judgment.

In order to first unify the receiver amplitude drop, the release boundary distance and the spatial position of the ground point into the same dimensional input, this paper first defines the basic feature vector as follows.

$$f_n = \left[\frac{U_{g,n}}{U_{0,n}}, \frac{U_{0,n} - U_{g,n}}{U_{0,n}}, \frac{U_{g,n} - U_r}{U_{0,n}}, \xi_n, \lambda_n\right]^T \tag{12}$$

where f_n represents the underlying eigenvector of the n sample, $U_{g,n}$ represents the track voltage at the receiver after grounding, $U_{0,n}$ represents the ungrounded reference voltage, U_r represents the release threshold, and ξ_n and λ_n represent the normalized distance ratio from the ground point to the transmitter and receiver, respectively. Equation (12) compresates the amplitude state, drop amplitude and boundary proximity into a unified vector, so that each sample has a comparable numerical structure at the input stage.

Considering that the track voltage shows continuous attenuation rather than a single point change along the section after grounding, the local attenuation gradient feature is further introduced to describe the spatial variation intensity.

$$g_n = \frac{1}{K}\sum_{q=1}^{K} \frac{\left|U_n(x_q + \Delta x) - U_n(x_q)\right|}{\Delta x} \tag{13}$$

where g_n represents the local voltage attenuation gradient of the n sample, $U_n(x_q)$ represents the voltage value at the discrete position x_q of the rail surface, and K is the number of discrete nodes participating in the statistics. Equation (13) reflects the spatial decline rate of the rail voltage after grounding, and can distinguish two different abnormal forms: "the overall decline is gentle" and "the local rapid drop".

Relying only on the voltage amplitude is still not enough to reflect the dual-rail coupling transmission imbalance, so it is also necessary to construct the imbalance index driven jointly by the potential difference and the current difference.

$$c_n = \frac{1}{l_n}\int_0^{l_n} \frac{(U_{1x} - U_{2x})^2 + \alpha(I_{1x} - I_{2x})^2}{U_{1x}^2 + U_{2x}^2 + \varepsilon}\, dx \tag{14}$$

Here, c_n represents the coupling imbalance coefficient, l_n is the section length,U_{1x} and U_{2x} represent the double rail potential to ground respectively, I_{1x} and I_{2x} represent the corresponding rail current, α is the weight coefficient of the current difference, ε is a small positive number to avoid the denominator being zero. Equation (14) transforms the asymmetric transmission state of the dual rail into a continuous integrable feature, which is used to describe the degree of coupling offset after the introduction of the ground branch.

In order to transcribe the proximity between the ground sample and the relay release boundary into a sortable quantity, this paper defines the anomaly proximity score and writes it in the following form.

$$p_n = \sigma\left(\beta_1 \frac{U_r - U_{g,n}}{U_r} + \beta_2 c_n + \beta_3 g_n + \beta_4 r_n\right) \tag{15}$$

Here, p_n represents the sample anomaly proximity score, $\sigma(\cdot)$is the Sigmoid function, r_n represents the reflux setting code, and β_1 to β_4 are the weight parameters of each feature component. Equation (15) jointly maps the release boundary distance, coupling imbalance degree, local gradient and topological condition to a continuous interval between zero and one, which is used to represent the strength level at which the sample is close to the anomaly display.

In order to avoid the many dimensions but scattered meanings of the subsequent model input, this paper summarizes the sources and functions of the main features in this section, as shown in Table 2.

Table 2: Feature composition of the ground "red light band" anomaly representation

Feature Category	Symbol	Data Source	Computational Meaning	Discriminative Role
Basic Amplitude Feature	(f_n)	Receiver-End Voltage and Reference Voltage	Describes the voltage drop ratio and release margin	Indicates anomaly intensity
Gradient Feature	(g_n)	Discrete Rail Voltage Sequence	Describes the spatial attenuation rate	Distinguishes local rapid drops
Coupling Feature	(c_n)	Potentials and Currents of the Two Rails	Describes transmission imbalance	Indicates the degree of grounding imbalance
Proximity Feature	(p_n)	Fusion of Amplitude, Gradient, and Topology	Describes the proximity of anomalies	Supports ranking and alarm generation
Operating Condition Encoding Feature	(r_n)	Return Current Settings and Grounding Modes	Describes boundary connection states	Distinguishes scenario sources

After obtaining the basic features, gradient features and coupling features, it is necessary to jointly encode the continuous variables and discrete operating conditions to form a unified anomaly representation matrix.

$$X_n = \mathrm{Concat}(f_n, g_n, c_n, p_n, e(r_n)) \tag{16}$$

Here, X_n represents the anomaly representation matrix of the n sample, $\mathrm{Concat}(\cdot)$ represents the feature concatenation operation, and $e(r_n)$ represents the embedding vector of the backflow setting and grounding mode. Equation (16) completes the final transliteration from physical parameters to abnormal signal representation, so that samples under different section lengths, different ballast resistance and different reflux conditions can enter the subsequent diagnosis and disposal model in a unified dimension.

Using the above feature extraction and abnormal representation, the receiver track voltage drop amplitude, release boundary proximity, dual-rail coupling imbalance state and return connection conditions are uniformly organized into the same feature space, different section length, different ballast resistance and different ground position of the samples therefore have a consistent input structure. The anomaly representation thus formed not only preserves the electrical transmission characteristics in the track circuit grounding scenario, but also enhances the comparability and discriminability between samples.

3.3 Intelligent calculation model for grounding "red light band" diagnosis and impedance grounding disposal

After the construction of the grounding condition sample and the representation of the abnormal signal, the task of the diagnostic model is no longer just to judge whether the track voltage at the receiver is below the release boundary, but to complete the anomaly identification, grounding structure correction and disposal strategy output at the same time in the same calculation link. The 25Hz phase-sensitive track circuit has obvious coupling transmission characteristics under the condition of maintenance and grounding. Once the temporary ground line is connected, a new electrical connection will be formed between the dual-rail signal loop and the traction return channel, and the track voltage at the receiving end will also be redistributed. If the existing single-rail grounding method is still adopted, the linkage influence among grounding position, reflux setting and section scale is difficult to be stably suppressed. Based on this, on the basis of state modeling and exception representation in the previous two sections, this section introduces an intelligent computing model oriented to disposal, which uniformly writes the impedance grounding structure, port correction relationship and disposal scoring rules into the decision-making process, so that the model output can not only describe the degree of the "red light band" approaching the release boundary, but also give a more suitable ground scheme for field implementation.

After completing the exception representation, the disposal model first needs to incorporate the grounding structure itself into the state update process. The temporary grounding method of the existing single rail will change the connection relationship between the signal loop and the traction return, and the track voltage at the receiving end will decrease significantly. In order to weaken the influence of this additional branch on signal transmission, this paper introduces a dual-rail impedance grounding structure, whose basic connection is shown in Fig. 3. The structure connects the dual rail and the traction return side simultaneously through two groups of coils, so that the track circuit signal current and the traction return flow form differential impedance responses in different paths. After this process, the loop impedance corresponding to the signal component is maintained at a high level, and the traction reflux is formed through the alien terminal to form a lower impedance channel, so as to take into account the signal transmission constraints and maintenance grounding requirements.

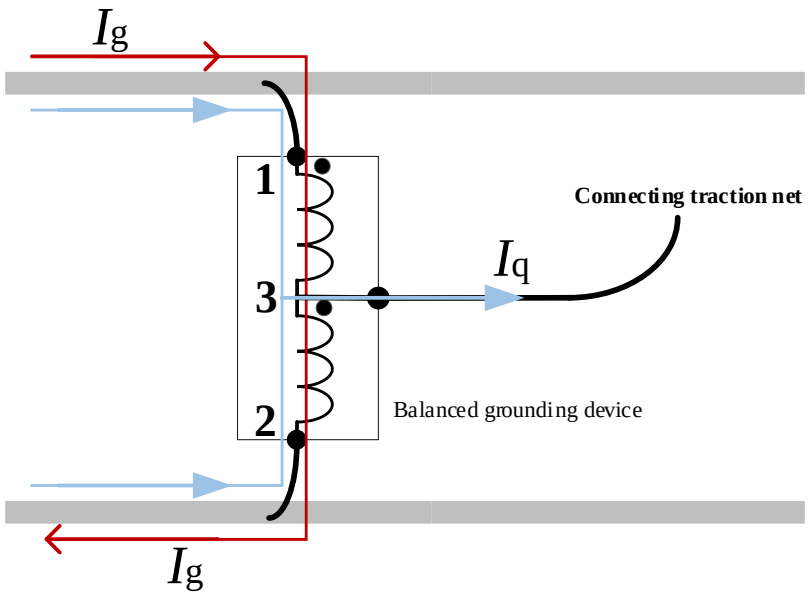

Figure 3: Schematic diagram of the impedance grounding scheme

When moving from the structure layer to the model layer, the track circuit is no longer defined by a single ground impedance, and the ground branches on both sides need to be included in the port condition. Fig. 4 illustrates the track circuit grounding model after impedance grounding. The boundary division of the transmitter, receiver, both sides of the ground point and the dual-rail branch is still consistent with the previous, but the middle connection relationship has been extended from a single ground point to a dual-impedance branch. In this way, instead of a single grounding action, the diagnostic model receives an information structure that simultaneously contains branch symmetries, impedance ratios, and boundary potential reallocations.

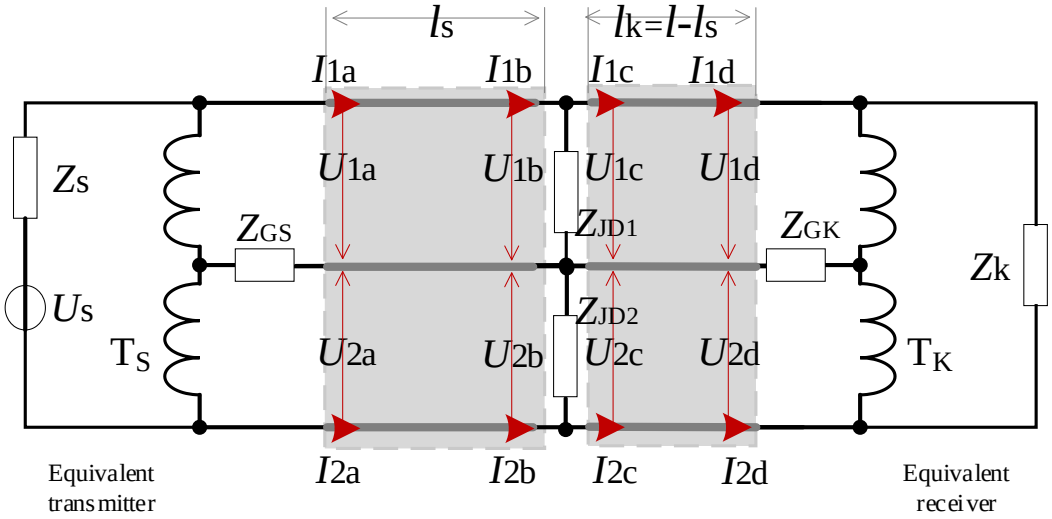

Figure 4: Track circuit grounding model based on impedance grounding scheme

In order to make the impedance grounding condition directly enter the transmission solution process, it is also necessary to write the two-branch grounding relationship into the intermediate port correction matrix and maintain the consistency between the front and back

boundary conditions and the recursive link, whose matrix expression is shown in Equation (17).

$$J = \begin{bmatrix} 1 & 0 & 0 & 0 \\ 0 & 1 & 0 & 0 \\ Z_{JD1}^{-1} & 0 & 1 & 0 \\ 0 & Z_{JD2}^{-1} & 0 & 1 \end{bmatrix} \tag{17}$$

Here, J is the port correction matrix under impedance grounding condition, and Z_{JD1} and Z_{JD2} represent the equivalent ground impedance formed by the dual rail through the impedance grounding device, respectively. Compared with the single ground point model, Equation (17) explicitly preserves the independent correction relation of the two rail branches, so that the grounding action is no longer compressed as a single-parameter disturbance, but enters the structural layer oriented to disposal calculation.

In order to write the separation ability of the grounding device for signal component and traction component into the subsequent decision-making process, the model also needs to define the impedance separation coefficient, which is used to measure the electrical differentiation degree of different loops under the same structure, and its calculation expression is shown in Formula (18).

$$\eta = \frac{\sqrt{R_{25}^2 + X_{25}^2}}{\sqrt{R_q^2 + X_q^2}} \tag{18}$$

Here, η represents the impedance separation coefficient, R_{25}^2 and X_{25}^2 represent the equivalent resistance and reactance of the 25Hz signal loop, respectively, and R_q and X_q represent the equivalent resistance and reactance of the traction reflux channel, respectively. The larger this coefficient is, the more obvious is the impedance distinction between the signal loop and the traction backflow, and the stronger is the protection ability of the grounding structure to the signal transmission.

After obtaining the impedance separation capability, it should be written into the receiver voltage reconstruction process together with the drop feature, coupling feature and gradient feature extracted above, so that different grounding schemes can be compared in the same framework. The estimated form is shown in Equation (19).

$$\widehat{U}_{g,n}^{(m)} = U_{0,n}(1 - \rho_n) + \gamma_1 \ln(1 + \eta_m) - \gamma_2 c_n - \gamma_3 g_n \tag{19}$$

where, $\widehat{U}_{g,n}^{(m)}$ represents the estimated receiver voltage value of the n sample under the m candidate grounding strategy, $U_{0,n}$ represents the ungrounded reference voltage, ρ_n represents the voltage reduction ratio, η_m represents the impedance separation coefficient corresponding to the strategy, c_n represents the coupling imbalance coefficient of the dual rail, g_n represents the voltage attenuation gradient of the rail surface, and γ_1 to γ_3 are the weight parameters. In Equation (19), the anomaly degree and the disposal structure are written into the same reconstruction expression, so that the model can directly estimate the voltage level at the receiver under different schemes.

Reconstruction voltage alone is not enough to complete candidate selection. Therefore, safety margin, impedance ratio, coupling balance and spatial attenuation should be jointly written into the comprehensive scoring function to form a rankable disposal result. The

comprehensive score is shown in equation (20).

$$S_n^{(m)} = \alpha_1 \frac{\hat{U}_{g,n}^{(m)} - U_r}{U_r} + \alpha_2 \frac{\eta_m}{1+\eta_m} + \alpha_3(1-c_n) + \alpha_4(1-g_n) \tag{20}$$

Here, $S_n^{(m)}$ represents the comprehensive disposal score of the n sample under the m strategy, U_r represents the relay release threshold, and α_1 to α_4 are the scoring weights. Equation (20) no longer relies on a single amplitude for sorting, but also considers whether the receiver voltage is out of the release boundary, whether the impedance separation is sufficient, whether the dual-rail transmission is balanced, and whether the spatial attenuation is suppressed, so it is more suitable for the strategy selection in the ground condition.

After completing the multi-strategy scoring, the model also needs to impose voltage safety constraints and impedance ratio constraints, and finally output the optimal grounding scheme. To this end, this paper writes the decision output as the optimal choice with constraints, and its expression is shown in equation (21).

$$m_n^* = \arg\max_{m \in \mathcal{M}} S_n^{(m)}, \quad \text{s.t.}\, \hat{U}_{g,n}^{(m)} \geq U_r + \delta, \eta_m \geq \eta_0 \tag{21}$$

Here, m_n^* represents the optimal disposal strategy corresponding to the n sample, M represents the set of candidate strategies, δ represents the safety margin, and η_0 represents the lower limit of impedance separation. Equation (21) shows that the final output is not simply to take the maximum score, but to select the optimal result from the candidate schemes after satisfying the dual constraints of voltage and impedance separation at the receiver. After this process, the model can not only identify the anomaly degree, but also give the disposal path.

Through the above modeling process, the impedance grounding structure, the port correction relationship, the receiver voltage reconstruction results, and the disposal scoring rules are uniformly organized into the same computing framework. Therefore, the originally scattered structural information, electrical information, and discriminant information in the ground "red band" scene form a continuous solution link. After this process, the output of the model no longer stays at the level of whether the anomaly occurs or not, but can further give the voltage response and disposal priority corresponding to different grounding strategies, so as to connect the diagnostic calculation and scheme selection in the grounding scenario of the track circuit.

4 Results and analysis

4.1 Problem model solution results and consistency analysis

In order to verify the solution reliability of the established problem model under different section lengths and different ballast resistance conditions, this paper compares the output results of the two algorithms under the same input conditions. Fig. 5 shows the simulation results of the rail surface voltage for the three categories of 1.2km, 0.6km and 0.3km sections under the condition of 0.6Ω·km and 6.0Ω·km ballast resistance.

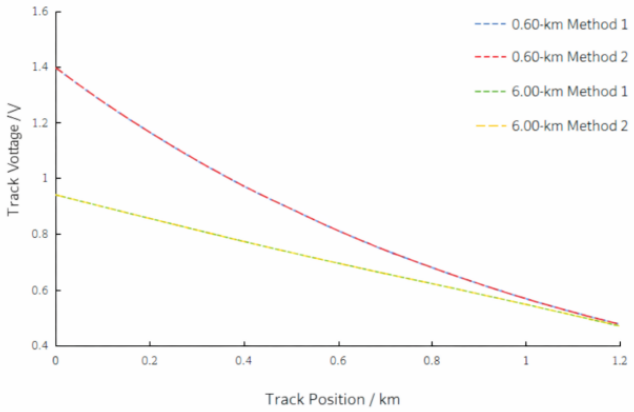

(a) Rail surface voltage simulation of 1.2km section

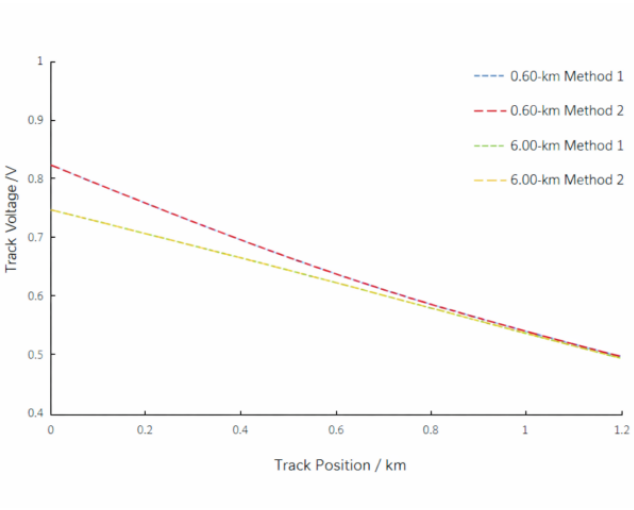

(b) Rail surface voltage simulation of 0.6km section

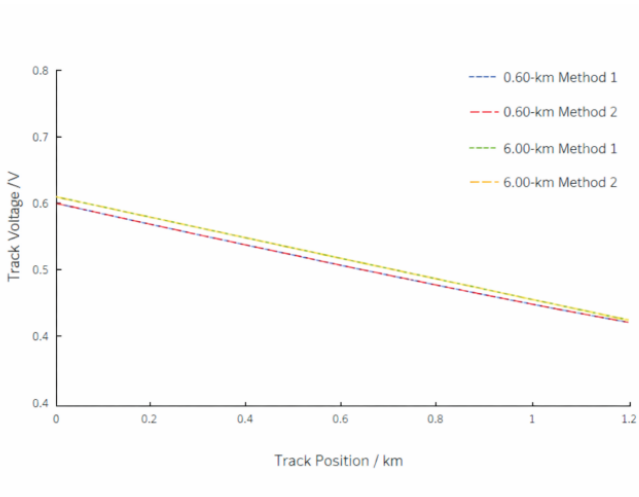

(c) Rail surface voltage simulation of 0.3km section

Figure 5: Comparison of rail surface voltage simulation data under the two algorithms

Fig. 5 shows that under the condition of 0.6Ω·km, the rail surface voltage of 1.2km section gradually decreases from 1.3970V to 0.4766V, and under the condition of 6.0Ω·km, it decreases from 0.9325V to 0.4680V. The numerical values of the two algorithms at each discrete node basically coincide, which indicates that the original transmission relationship of the six-terminal network is not changed after finite difference discretization, and the recurrence chain between the sender and the receiver remains stable. For the subsequent grounding "red band" analysis, this consistency means that the model output is reproducible, and subsequent comparisons under different reflux conditions and grounding positions are based on the same numerical value.

To further show the error distribution under different parameter combinations, Fig. 6 shows the node error thermal results of the two algorithms under the conditions of three types of section lengths and two types of ballast resistance.

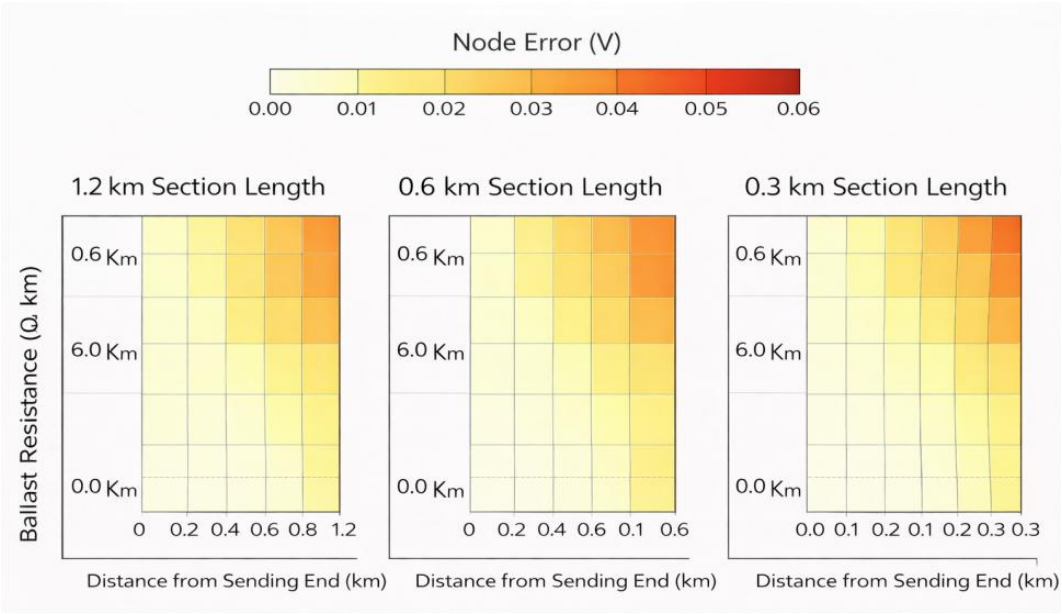

Figure 6: Node error distribution diagram under different section length and ballast resistance conditions

Fig. 6 shows that the errors of the two algorithms are smaller overall at each node. Taking the 1.2km section as an example, under the condition of 0.6Ω·km, the rail surface voltage of the two algorithms at the starting position is 1.3970377617V, and the end position is 0.4765844515V. Under the condition of 6.0Ω·km, the starting position is 0.9324564238V, and the ending position is 0.4679989416V. Under the combination of 0.3km and 6.0Ω·km, the results of each node are also consistent, and there is no local sudden increase or continuous offset, indicating that the short section and high ballast resistance do not cause numerical instability, and the model still maintains stable solution ability under adverse boundaries.

In order to ensure that the above consistency analysis and the experimental boundary remain corresponding, Table 3 lists the length of the six groups of section samples, ballast resistance, feed end position, simulation value, actual adjustment value and error.

Table 3: Table of configuration parameters for each section in the experiment

Section No.	Length / km	Ballast Resistance / Ω·km	BG25 Level at Sending End / V	Simulated Value / V	Actual Adjusted Value / V	Error / %
I-A	1.2	0.6	8.80	15.0170	15.671	4.355
I-B	1.2	6.0	4.84	15.0120	15.387	2.497
II-A	0.6	0.6	4.84	15.0021	15.487	3.232
II-B	0.6	6.0	3.96	15.0112	15.594	3.882
III-A	0.3	0.6	3.96	15.0180	15.270	1.678
III-B	0.3	6.0	3.52	15.0069	15.431	2.826

Table 3 shows that the simulation values of the 1.2km section under the conditions of 0.6Ω·km and 6.0Ω·km are 15.0170V and 15.0120V, respectively, and the experimental adjustment values are 15.671V and 15.387V, respectively, under the conditions of no reflux and no grounding. In 0.6km section, the simulation values are 15.0021V and 15.0112V, and the experimental values are 15.487V and 15.594V under two conditions. The corresponding simulation values of the 0.3km section are 15.0180V and 15.0069V, and the experimental values are 15.270V and 15.431V. The sample errors of the six groups were all controlled within 5%, indicating that there is a good correspondence between the simulation boundary, the equipment parameters and the experimental setup.

Based on the above results, it can be seen that the problem model maintains a stable solution ability under multi-section and multi-ballast conditions, the agreement between the finite difference method and the control algorithm is high, and the initial boundary of the experiment is also consistent with the simulation input.

4.2 Key influencing factors of grounding "red light band" and analysis of discrimination results

On the premise that the model solution remains consistent, the key influencing factors of the ground "red light band" can be further identified by the track voltage variation at the receiver. In order to compare the influence of section length, ballast resistance and reflux setting conditions on the discrimination results, Fig. 7 shows the simulation results of the track voltage at the receiving end of the three types of sections under different grounding positions。

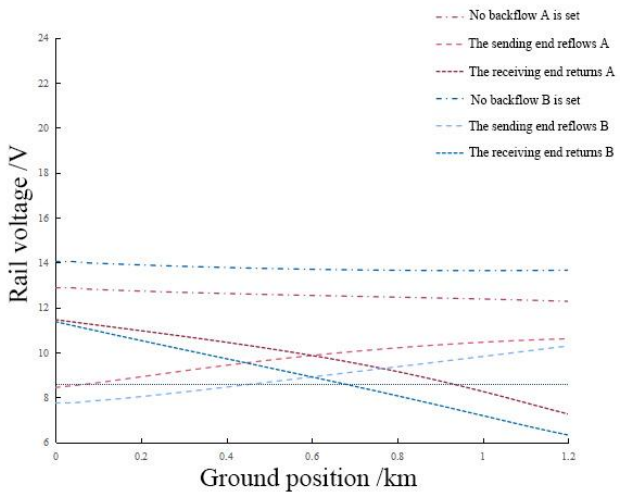

(a) Simulation of track voltage after grounding of 1.2km section

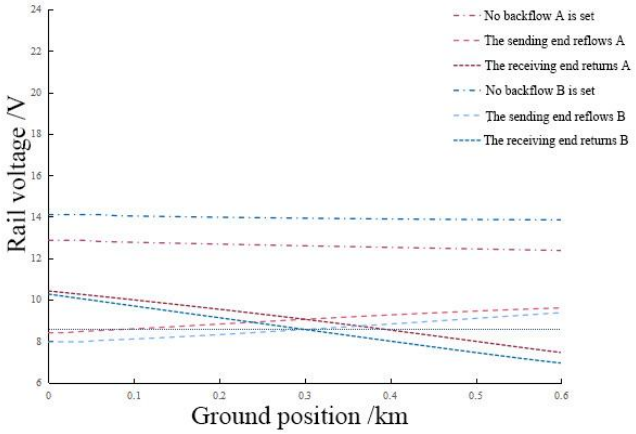

(b) simulation of track voltage after grounding of 0.6km section

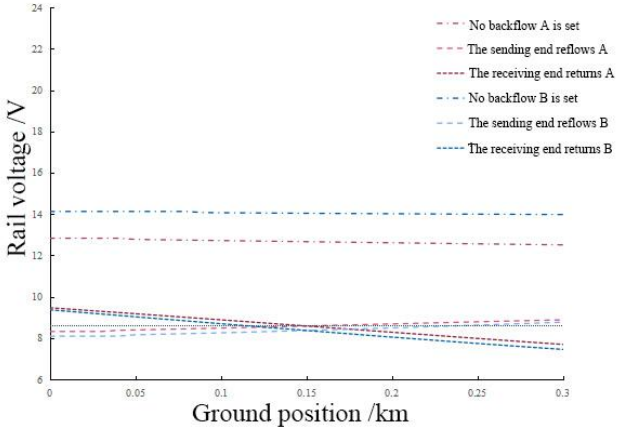

(c) simulation of track voltage after grounding of 0.3km section

Figure 7: Comparison of simulation data of track voltage after grounding under different conditions

Fig. 7 shows that the track voltages of 1.2km, 0.6km and 0.3km sections under 0.6Ω·km condition are 15.0170V, 15.0021V and 15.0180V, respectively, when ungrounded. Under the condition of 6.0Ω·km, the three sections are 15.0121V, 15.0112V and 15.0069V respectively. After grounding, the maximum reduction of the three sections without reflow is 18.245%, 17.575% and 16.698%, respectively, and the corresponding voltages are still higher than the 8.6V release value. Under the condition of backflow at the feed end, the maximum reduction of the three types of sections reaches 43.768%, 44.014%, 44.601% at 0.6Ω·km, and 48.332%, 46.979%, 46.063% at 6.0Ω·km. Under the condition of receiving end reflux, the maximum decline further expanded to 51.665%, 50.380%, 48.759% and 57.881%, 53.804%, 48.759%. These data indicate that the reflux setting has the most direct effect on triggering the abnormal display, and the section length and ballast resistance determine the extent of the release interval extension.

Fig. 8 summarizes the distribution of discriminative regions corresponding to different reflux modes and ground point locations.

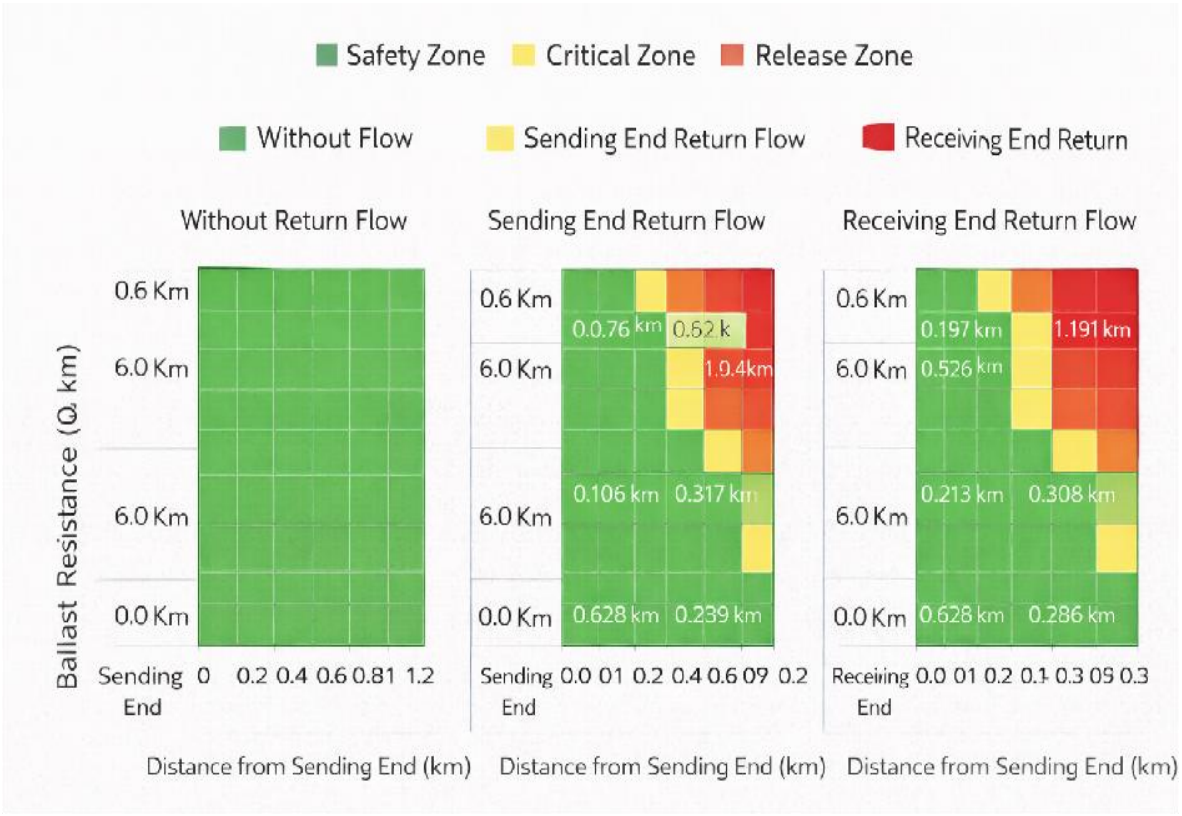

Figure 8: The distribution map of the discriminant area for different reflux modes and ground point locations

Fig. 8 shows that the rail voltage is higher than 8.6V after grounding in all sections without backflow. Under the condition of 0.6Ω·km, the 1.2km, 0.6km and 0.3km sections enter the release zone within 0.076km, 0.106km and 0.157km from the feed end, respectively. The corresponding values are 0.462km, 0.317km and 0.239km under the condition of 6.0Ω·km. When the receiver is reflow, the corresponding distances are 0.271km, 0.213km and 0.153km under 0.6Ω·km condition, and 0.526km, 0.308km and 0.186km under 6.0Ω·km condition. The short section has a higher proportion of the release area after setting the reflux, indicating that the reflux direction determines the position of the low voltage area, and the length of the section and the ballast resistance jointly determine the scope of the release area.

In order to correspond the simulation discrimination with the measured performance, Table 4 lists the experimental data after grounding in the existing way.

Table 4: Experimental data table of track voltage after grounding in existing ways (indicates "red light band" display in the experiment)*

Section sequence number	Position of ground	No backflow is set			The sending end reflows			Backflow at the receiving end		
		Simulation value /V	The experimental value /V	Error /%	Simulation value /V	The experimental value /V	Error /%	Simulation value /V	The experimental value /V	Error /%
I-A	End of delivery	12.881 3	13.447	4.392	8.444 4	7.801*	-7.619	11.461 0	12.344	7.705
I-A	End of receiver	12.277 2	12.821	4.429	10.611 4	9.259	-12.769	7.258 5	8.104*	11.648
I-B	End of delivery	14.049 4	13.498	-3.925	7.756 4	7.429*	-4.222	11.372 5	12.171	7.021
I-B	End of receiver	13.662 1	14.000	2.473	10.292 9	8.901	-13.523	6.322 9	6.819*	7.846
II-A	End of delivery	12.858 3	13.885	7.985	8.399 1	8.664*	3.154	10.413 7	11.000	5.630
II-A	End of receiver	12.365 5	11.887	-3.870	9.595 8	9.771	1.826	7.444 1	8.046*	8.086
II-B	End of delivery	14.098 3	13.112	-6.996	7.959 1	8.304*	4.333	10.261 1	10.120	-1.375
II-B	End of receiver	13.844 1	12.476	-9.882	9.366 3	10.110	7.940	6.934 5	7.380*	6.424
III-A	End of delivery	12.832 7	11.963	-6.777	8.319 8	8.114*	-2.474	9.468 4	9.002*	-4.926
III-A	End of receiver	12.510 3	11.829	-5.446	8.883 9	8.287*	-6.719	7.695 3	7.045*	-8.451
III-B	End of delivery	14.128 0	13.988	-0.991	8.094 3	8.112*	0.219	9.369 2	9.047*	-3.439
III-B	End of receiver	13.979 7	14.462	3.450	8.769 2	8.890*	1.378	7.454 4	8.145*	9.264

Table 4 shows that in sections I-A, I-B, II-A and II-B, the ground "red light band" is observed when the transmitter is backflowing and the transmitter is grounded, and the receiver is backflowing and the receiver is grounded. In the short sections III-A and III-B, as long as the backflow connection is present, the abnormal display may occur regardless of the ground at the transmitter or the ground at the receiver. The statistical mean error of the whole group of experiments relative to the simulation is 0.050%, and the mean square error is 6.727%. This result shows that the key influencing factors reflected in Fig. 7 not only exist in the simulation level, but also can be directly observed in the experiment.

Based on the above results, it can be clearly obtained that the reflux setting determines the location and scope of the abnormal occurrence, the section length and the ballast resistance determine the expansion degree of the release area, and the three together constitute the key influencing factors of the grounding "red light belt". The results in this section provide a clear reference for the output comparison of the impedance grounding scheme in the next section.

4.3 Output results and experimental verification of the impedance grounding scheme

After completing the solution consistency verification and key influencing factors identification in the previous two sections, this section further analyzes the output results of the impedance grounding scheme and verifies the effectiveness of the scheme through experimental data. Fig. 9 shows the simulation results of the track voltage after grounding under different section lengths, different ballast resistors and different reflux Settings after the implementation of the impedance grounding scheme.

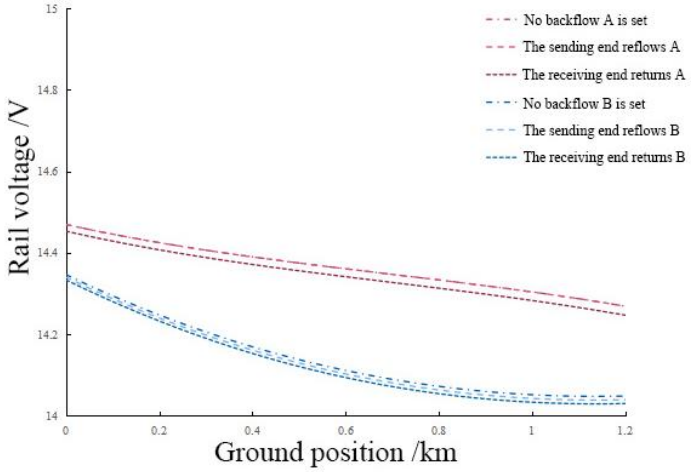

(a) Simulation of track voltage after grounding of 1.2km section

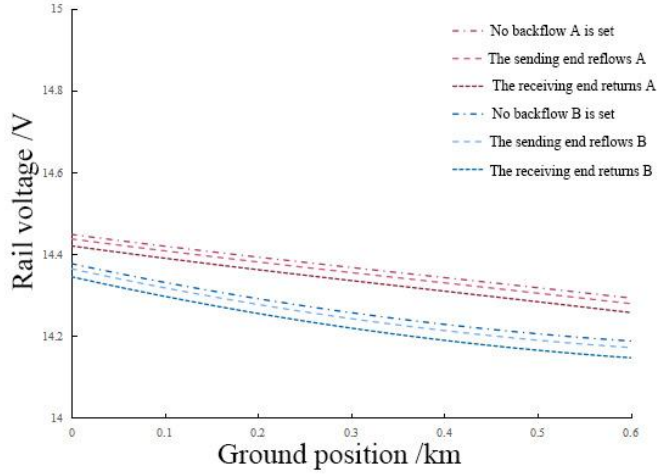

(b) simulation of track voltage after grounding of 0.6km section

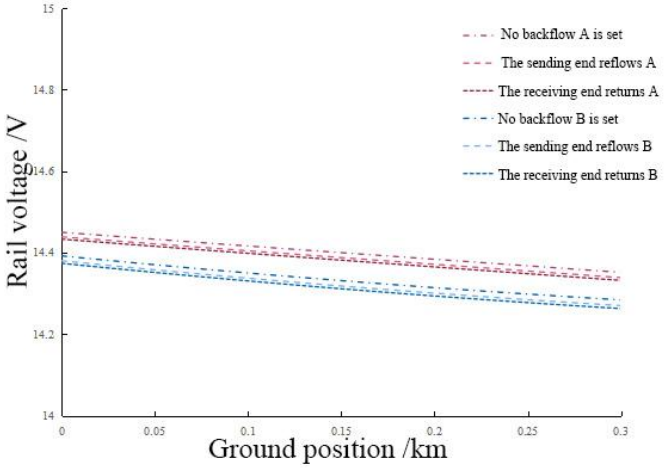

(c) simulation of track voltage after grounding of 0.3km section

Figure 9: Comparison of track voltage simulation data after grounding under impedance grounding scheme

Fig. 9 shows that the maximum reduction of 1.2km, 0.6km and 0.3km sections is 4.980%, 4.728% and 4.435% respectively under 0.6Ω·km condition, and 6.423%, 5.487% and 4.814% respectively under 6.0Ω·km condition when the impedance earthing scheme is adopted. Under the conditions of the return of the feed end, the maximum reduction of the two types of ballast resistance is 5.028%, 4.820%, 4.522% and 6.483%, 5.592%, 4.908%; Under the condition of receiving end reflux, the corresponding maximum decreases were 5.127%, 4.965%, 4.567% and 6.546%, 5.760%, 4.956%, respectively. In the whole set of simulations, the average decrease of the rail voltage under various conditions is 5.230%, and the single decrease value does not exceed 1.0V. The impedance grounding scheme significantly shrinks the anomaly region compared to the large drop into the 8.6V release boundary under the existing mode.

To verify the simulation output in Fig. 9, Table 5 lists the experimental data after adopting impedance grounding.

Table 5: Experimental data sheet of track voltage after using impedance grounding

Section sequence number	Position of ground	No backflow is set			The sending end reflows			Backflow at the receiving end		
		Simulation value /V	The experimental value /V	Error /%	Simulation value /V	The experimental value /V	Error /%	Simulation value /V	The experimental value /V	Error /%
I-A	End of delivery	14.469 6	14.202	-1.849	14.464 2	14.157	-2.124	14.453 2	14.285	-1.164
I-A	End of receiver	14.269 1	14.071	-1.388	14.261 9	13.998	-1.850	14.247 1	13.981	-1.868
I-B	End of delivery	14.346 6	14.355	0.059	14.340 2	14.173	-1.166	14.333 6	14.004	-2.299
I-B	End of receiver	14.048 7	14.377	2.337	14.039 6	14.501	3.286	14.030 3	13.997	-0.237
II-A	End of delivery	14.448 3	14.143	-2.113	14.437 4	14.752	2.179	14.420 2	14.272	-1.028
II-A	End of receiver	14.292 8	13.976	-2.217	14.279 0	14.074	-1.436	14.257 3	14.099	-1.110
II-B	End of delivery	14.376 8	14.884	3.528	14.364 4	14.072	-2.036	14.344 8	14.085	-1.811
II-B	End of receiver	14.187 6	13.974	-1.506	14.171 7	13.854	-2.242	14.146 6	14.321	1.233
III-A	End of delivery	14.450 2	14.071	-2.624	14.439 0	13.851	-4.072	14.433 2	14.280	-1.061
III-A	End of receiver	14.351 9	13.217	-7.908	14.338 9	13.897	-3.082	14.332 2	14.484	1.059
III-B	End of delivery	14.392 3	14.090	-2.100	14.380 3	14.007	-2.596	14.374 1	13.718	-4.564
III-B	End of receiver	14.284 4	14.155	-0.906	14.270 4	14.071	-1.397	14.263 1	14.109	-1.080

Table 5 shows that the mean value of the post-grounding voltage of the six groups of sections under the condition of impedance grounding reaches 14.284V, the statistical mean value of the relative simulation error is -1.310%, and the mean square error is 2.139%. From the samples of each group, the overall rail voltage remained at a high level after grounding, and no "red light band" was observed in the experiment. The results show that the output of the disposal model given in Chapter 3 maintains a good consistency with the actual plant performance, and the scheme has the foundation of engineering implementation, rather than the theoretical results at the simulation level.

To further illustrate the role of each component in the disposition model on the final output, the ablation experiment results are introduced in this section, as shown in Table 6.

Table 6: Ablation experimental results for the impedance grounded disposal model

Model Setting	Average Reduction / %	Mean Voltage after Grounding / V	Abnormal Display
Complete Model	5.230	14.284	No
Without Dual-Rail Impedance Branch	11.742	12.931	Yes
Without Impedance Separation Constraint	8.964	13.506	No
Without Safety Margin Constraint	7.885	13.742	Critical

Table 6 shows that the full model maintains the best performance in the three indicators of average drop, average voltage after grounding, and abnormal display suppression. After removing the dual-rail impedance branch, the average drop rises to 11.742%, the average voltage drops to 12.931V, and the abnormal display appears again. After removing the impedance separation constraint, although no abnormal display can be maintained, the output is more sensitive to the reflux boundary. After removing the safety margin constraint, although the mean value of the voltage after grounding reaches 13.742V, it is near the boundary and the stability decreases significantly.

Taking the above results together, it can be seen that the effectiveness of the impedance grounding scheme comes from the joint action of structural modification, impedance separation and safety margin rather than single parameter adjustment. The proposed scheme not only compresses the track voltage drop significantly in the simulation, but also maintains high consistency and stability in the experiment, so it can be used as an effective output result of the ground "red light band" disposal.

5 Conclusion

In this paper, a complete computational chain from state modeling, anomaly representation to disposal output is constructed around a 25Hz phase-sensitive track circuit grounded "red light band" scenario. The study is based on the six-terminal network transmission relationship, the grounding position, section length, ballast resistance and reflux Settings and other working conditions parameters are uniformly written into the state space, on this basis, the finite difference and cascaded recurrence method is used to complete the track voltage solution, and further form the characteristic representation structure for grounding anomaly recognition.

Combining the simulation calculation and experimental comparison under different working conditions, it can be seen that the established model can stably describe the change process of rail voltage after grounding, and the results of the two algorithms on the corresponding nodes are consistent, indicating that the discrete solution does not damage the original transmission chain. Further analysis shows that there is a significant coupling relationship between the formation of the grounding "red belt" and the reflux setting, section length and ballast resistance, which is closer to the most adverse working condition when the short section, high ballast resistance and unilateral reflux channel are stacked.

Based on the above rules, the dual-rail impedance grounding scheme is proposed and written into the decision output process of the disposal model. The simulation results show that the average decrease of rail voltage after grounding is 5.230%, and the decrease value is less than 1.0V. Experimental results show that the mean value of the voltage after grounding reaches 14.284V, the statistical mean value of the relative simulation error is -1.310%, and the mean square error is 2.139%, which shows that the scheme maintains good stability and consistency in the model layer and device layer. For engineering applications, this result

makes the coupling relationship between ground protection and signal transmission clearer, and also provides a reusable path for automatic analysis and auxiliary disposal of similar scenarios in the station.

There are still some limitations in this paper. At present, the section types covered by the sample are still mainly concentrated in typical station scenarios, and have not been extended to one-to-two delivery, dynamic train occupancy and more complex traction coupling conditions. Although the anomaly representation has incorporated spatial gradient and boundary constraints, the representation of time-varying disturbances and online updates is still static. In the future, the state space can be extended based on the measured data in multiple scenarios, and the online learning, graph structure update and digital twin simulation mechanisms can be introduced to make the model have stronger migration ability, adaptive ability and field deployment ability. In addition, the parameter weights of the current scheme are still mainly off-line calibration, and there is still room for improvement in the real-time response ability to seasonal bed state fluctuations, harmonic disturbances and maintenance organization differences. Subsequently, edge acquisition and online parameter inversion can be combined to realize continuous self-calibration and engineering deployment of the model in the field environment.

Funding

This work was supported by the Key R&D Project of the National Energy Group (CEZB220207860) and the Science and Technology Research and Development Plan of China Railway Qinghai-Tibet Group Co., Ltd. (QZ2021-D01).

References

[1] Lian H, Wang X, Sharma A, et al. Application and study of artificial intelligence in railway signal interlocking fault[J]. Informatica, 2022, 46(3).

[2] Yang Y. Fault Diagnosis Technology of Railway Signal Equipment based on Improved FP-Growth Algorithm[J]. International Journal of Advanced Computer Science and Applications, 2022, 13(12).

[3] Hu X, Cao Y, Tang T, et al. Data-driven technology of fault diagnosis in railway point machines: Review and challenges[J]. Transportation Safety and Environment, 2022, 4(4): tdac036.

[4] Li M, Hei X, Ji W, et al. A fault-diagnosis method for railway turnout systems based on improved autoencoder and data augmentation[J]. Sensors, 2022, 22(23): 9438.

[5] Cao Y, Sun Y, Xie G, et al. A sound-based fault diagnosis method for railway point machines based on two-stage feature selection strategy and ensemble classifier[J]. IEEE Transactions on Intelligent Transportation Systems, 2021, 23(8): 12074-12083.

[6] Sun Y, Cao Y, Li P. Contactless fault diagnosis for railway point machines based on multi-scale fractional wavelet packet energy entropy and synchronous optimization strategy[J]. IEEE Transactions on Vehicular Technology, 2022, 71(6): 5906-5914.

[7] Cao Y, Ji Y, Sun Y, et al. The fault diagnosis of a switch machine based on deep random

forest fusion[J]. IEEE Intelligent Transportation Systems Magazine, 2022, 15(1): 437-452.

[8] Chen X, Liu H, Duan Z. Railway switch fault diagnosis based on multi-heads channel self attention, residual connection and deep CNN[J]. Transportation Safety and Environment, 2023, 5(1): tdac045.

[9] Sun Y, Cao Y, Liu H, et al. Condition monitoring and fault diagnosis strategy of railway point machines using vibration signals[J]. Transportation Safety and Environment, 2023, 5(2): tdac048.

[10] Zhang M, Cao Y, Sun Y, et al. Vibration signal-based defect detection method for railway signal relay using parameter-optimized VMD and ensemble feature selection[J]. Control Engineering Practice, 2023, 139: 105630.

[11] Li C, Mu Z. Analysis platform of rail transit vehicle signal system based on data mining[J]. Informatica, 2023, 47(3).

[12] Zhou F, Li F. Fault diagnosis of a computer interlocking system for railway signal control[J]. Engineering Research Express, 2023, 5(4): 045034.

[13] Wang Z, Wang N, Zhang H, et al. Segmentalized mRMR features and cost-sensitive ELM with fixed inputs for fault diagnosis of high-speed railway turnouts[J]. IEEE Transactions on Intelligent Transportation Systems, 2023, 24(5): 4975-4987.

[14] Heinrich M, Gölz A, Arul T, et al. Rule-based anomaly detection for railway signalling networks[J]. International Journal of Critical Infrastructure Protection, 2023, 42: 100603.

[15] Chen C, Li X, Huang K, et al. A convolutional autoencoder based fault detection method for metro railway turnout[J]. CMES-Computer Modeling in Engineering and Sciences, 2023, 136(1): 471-485.

[16] Lao Z, He D, Jin Z, et al. Few-shot fault diagnosis of turnout switch machine based on semi-supervised weighted prototypical network[J]. Knowledge-Based Systems, 2023, 274: 110634.

[17] Reetz S, Neumann T, Schrijver G, et al. Expert system based fault diagnosis for railway point machines[J]. Proceedings of the Institution of Mechanical Engineers, Part F: Journal of Rail and Rapid Transit, 2024, 238(2): 214-224.

[18] Xiao S, Feng Q, Li X, et al. Research on intelligent fault diagnosis for railway point machines using deep reinforcement learning[J]. Transportation Safety and Environment, 2024, 6(4): tdae007.

[19] Yang N, Zhang Y, Zuo J, et al. Fault Diagnosis Method for Railway Signal Equipment Based on Data Enhancement and an Improved Attention Mechanism[J]. Machines, 2024, 12(5): 334.

[20] Sugiana A, Cahyadi W A, Yusran Y. Current-signal-based fault diagnosis of railway point machines using machine learning[J]. Applied Sciences, 2023, 14(1): 267.